




# 3D printing of hydroxyapatite/tricalcium phosphate scaffold with hierarchical porous structure for bone regeneration

Xiangjia Li<sup>1</sup> · Yuan Yuan<sup>2</sup> · Luyang Liu<sup>3</sup> · Yuen-Shan Leung<sup>1</sup> · Yiyu Chen<sup>4</sup> · Yuxing Guo<sup>2,5</sup> · Yang Chai<sup>2</sup> · Yong Chen<sup>1,4</sup> 

Received: 7 October 2019 / Accepted: 4 December 2019  
© Zhejiang University Press 2019

## Abstract

Three-dimensional (3D)-printed scaffolds have attracted considerable attention in recent years as they provide a suitable environment for bone cell tissue regeneration and can be customized in shape. Among many other challenges, the material composition and geometric structure have major impacts on the performance of scaffolds. Hydroxyapatite and tricalcium phosphate (HA/TCP), as the major constituents of natural bone and teeth, possess attractive biological properties and are widely used in bone scaffold fabrication. Many fabrication methods have been investigated in attempts to achieve HA/TCP scaffolds with microporous structure enabling cell growth and nutrient transport. However, current 3D printing methods can only achieve the fabrication of HA/TCP scaffolds with certain range of microporous structure. To overcome this challenge, we developed a slurry-based microscale mask image projection stereolithography, allowing us to form a HA/TCP-based photocurable suspension with complex geometry including biomimetic features and hierarchical porosity. Here, the curing performance and physical properties of the HA/TCP suspension were investigated, and a circular movement process for the fabrication of highly viscous HA/TCP suspension was developed. Based on these investigations, the scaffold composition was optimized. We determined that a 30 wt% HA/TCP scaffold with biomimetic hierarchical structure exhibited superior mechanical properties and porosity. Cell proliferation was investigated in vitro, and the surgery was conducted in a nude mouse in vivo model of long bone with cranial neural crest cells and bone marrow mesenchymal stem cells. The results showed our 3D-printed HA/TCP scaffold with biomimetic hierarchical structure is biocompatible and has sufficient mechanical strength for surgery.

**Keywords** 3D printing · Slurry stereolithography · Scaffold · HA/TCP · Hierarchical porosity

## Introduction

Natural bone tissue is composed of hierarchical porous structures that support cell growth, provide space for nutrient transport, and endure different types of ambient load (Fig. 1a) [1]. Traditionally, critical-sized or non-union bone defects are treated by surgically implanting a biocompatible bone graft substitute made of a tough but light material such as metal, composite, or high-stress polymer [2]. Even though this kind of implants withstands the mechanical loading and meets aesthetic appeal [2], there are a lot of problems in the long-term use of such kind of implants, e.g., potential migration and translocation, allergic reactions, secondary surgeries, etc. [3, 4]. In order to provide a truly biological solution to healing critical-sized bone defects, researchers endeavor to regenerate bone tissue by utilizing a three-dimensional (3D) scaffold cultured with the cells and growth factors [5]. In the 3D scaffold, the porous structure provides sufficient

✉ Yong Chen  
yongchen@usc.edu

<sup>1</sup> Epstein Department of Industrial and Systems Engineering, University of Southern California, Los Angeles, USA

<sup>2</sup> Center for Craniofacial Molecular Biology, University of Southern California, Los Angeles, USA

<sup>3</sup> Department of Chemical Engineering and Material Science, University of Southern California, Los Angeles, USA

<sup>4</sup> Department of Aerospace and Mechanical Engineering, University of Southern California, Los Angeles, USA

<sup>5</sup> Department of Oral and Maxillofacial Surgery, Peking University School and Hospital of Stomatology, Beijing, China

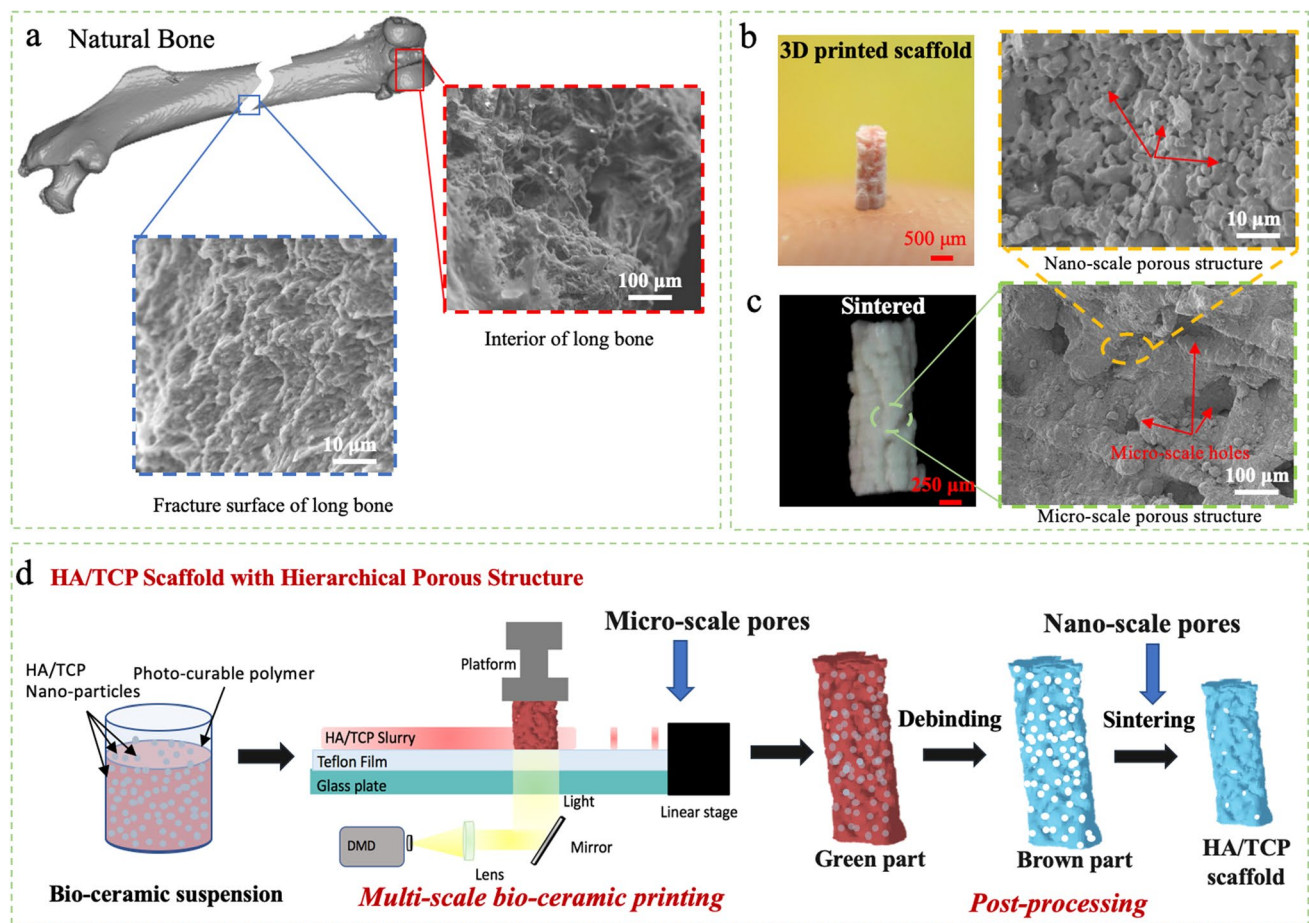


**Fig. 1** Schematic diagram of 3D-printed HA/TCP scaffold with bioinspired hierarchical porous structure. **a** A nude mouse long bone image; **b** microscopy of printed green part of biomimetic HA/TCP scaffold; **c** microscope and SEM images of biomimetic HA/TCP scaffold

fold with micro- and submicron-scale pores after sintering; and **d** the developed 3D printing process for the fabrication of HA/TCP scaffold with hierarchical porous structure

space for cell attachment, and the crisscrossed inner pore network enables blood vessels to deliver nutrition throughout the scaffold [2]. In addition, the scaffold material also has positive effects on bone tissue regeneration and is biocompatible, nontoxic, and biodegradable on a favorable timescale for bone healing. Overall, both the material and structure of the scaffold play critical roles in the successful healing of bone defects [8, 9].

Hydroxyapatite (HA) nanopowder shows promising properties for tissue engineering applications because it is able to promote the adhesion and proliferation of bone-forming cells, which can be incorporated into the biodegradable polymer composite [10] or deposited on biocompatible substrates [11]. Tricalcium phosphate (TCP), one of the main components of natural human bone, is a biodegradable bio-ceramic that is widely used to fabricate bone graft substitutes for orthopedic surgery [2, 3, 7, 12]. Many different techniques, such as freezing casting [5, 13], foam replica method [6], solvent casting [14], particle leaching [15], high-pressure

pressing [16], and injection molding [17], have been developed to fabricate HA/TCP-based 3D scaffolds. However, there are certain limitations on geometric shapes of HA/TCP scaffolds fabricated by these methods (Table 1). It is difficult to construct customized HA/TCP scaffolds with controllable hierarchical porous structures [2, 7].

Recent advances in bio-printing have shown promise for overcoming these limitations and hold the potential for biomedical engineers to design customized scaffolds based on patient-specific requirements [7, 10]. Several 3D printing methods were developed for the manufacturing of HA/TCP scaffolds with specially designed geometric structures [12, 21, 23–29]. For example, PCL/TCP- and PCL/HA-based composite scaffolds were fabricated by fused deposition modeling (FDM), with a fiber diameter greater than 200  $\mu\text{m}$  [23]. A hybrid process was developed to achieve a high percentage of HA/TCP concentration. Specifically, HA or TCP powder mixed with the binder was used in the 3D printing process to form a 3D object (referred to as the “green

**Table 1** Comparison of the 3D-printed HA/TCP-based scaffold with other works

Method	Material	Porous structure size	Porous structure shape	Porosity (%)	Mechanical strength (MPa)	Ref.
Freeze-casting	HA/TCP	40–200 $\mu\text{m}$	Uncontrollable	31.4–72.5	1.95–2.98	[5, 13]
Foam replica method	HA/TCP	500 $\mu\text{m}$	Uncontrollable	87	0.05	[6]
Solvent casting	PGA/TCP	483 $\mu\text{m}$	Uncontrollable	88.4		[14]
Particle leaching	PLA/ $\beta$ -TCP	300–420 $\mu\text{m}$	Uncontrollable	50	4–6	[15]
High-pressure pressing	HA	1 $\mu\text{m}$	Uncontrollable	20–40	40–100	[16]
Injection molding	HA/EVA/PA66	200–600 $\mu\text{m}$	Uncontrollable	60–75	5–10	[17]
Fused deposition modeling (FDM)	TCP	300–500 $\mu\text{m}$	Mesh matrix (Controllable)	29–44	0.24–1.44	[18]
Powder binder jetting	TCP	400–800 $\mu\text{m}$ and $\leq 5 \mu\text{m}$	Mesh matrix (Controllable)	27–50	3–11	[19, 20]
Vat photo-polymerization	HA	1000 $\mu\text{m}$	Mesh matrix (Controllable)	27	4.3–11.2	[21]
Extrusion-based printing	HA/TCP	50–580 $\mu\text{m}$	Mesh matrix (Controllable)	30–70	20–100	[22]
Our $\mu\text{MIP-SL}$	HA/TCP	20–1000 $\mu\text{m}$ and $\leq 5 \mu\text{m}$	Free-form structure (Controllable)	20–80	15	

part”), and then, the binder was removed by post-processing, such as high-temperature sintering or chemical dissolution [21, 24, 29–33]. For instance,  $\beta$ -TCP paste, consisting of  $\beta$ -TCP powder and PVA solution, was first used to create a 3D mesh matrix using the injection-based printing, and a final mesh-shaped  $\beta$ -TCP scaffold was obtained after sintering at 1100 °C [26]. Similarly, an HA/TCP scaffold was fabricated using an extrusion-based printing process, and the polymeric additives inside were burned off by heating to 625 °C [29]. After the post-processing, only submicron-sized pores were generated between HA/TCP particles [21, 29–35], and such an inner structure is too dense to provide cells with necessary space for the exchange of nutrients during growth. Therefore, it is necessary to build HA/TCP scaffolds with hierarchical porous structure ranging from hundreds of microns to submicron level, to maintain stable nutrient transport and cell metabolism [8, 18]. However, most 3D printing processes can only fabricate macroscale HA/TCP scaffolds with holes on the scale of hundreds of microns (Table 1). Due to current limitations on printing resolution, microscale features smaller than 100  $\mu\text{m}$  are difficult to fabricate [28–34]. Furthermore, there are limitations on the geometric shapes of HA/TCP scaffolds fabricated using powder binder jetting and extrusion-based 3D printing, because HA/TCP-based material (powder or filament) must be stacked layer by layer to avoid distortion while supporting material extrusion [28–34]. To address the increasing demand for HA/TCP scaffolds with large porosity and hierarchical porous distribution for applications in bone tissue regeneration [36, 37], it is of great importance to develop a 3D printing process that can accommodate these needs [38–42].

Unlike most other 3D printing methods, the mask image projection-based stereolithography (MIP-SL) has the capability to fabricate free-form surface models with relatively

complex inner structures [43–47]. Using the macroscale MIP-SL process, photopolymers mixed with bio-ceramic can be first solidified using high-resolution light projection, and later, the photocurable polymer can be completely burned off with a high-temperature sintering process [21, 48, 49]. The processing resolution of macroscale MIP-SL, however, cannot fulfill the requirement on hierarchical porous structure fabrication for bone tissue engineering. In this study, we developed a microscale mask image projection stereolithography ( $\mu\text{MIP-SL}$ ) process with a special slurry feeding module that allows the fabrication of HA/TCP scaffold with hierarchical porous structure (Fig. 1c). Nanoscale HA/TCP particle was used, and the curing performance and physical properties of the HA/TCP suspension were investigated. With the help of a high-resolution optical system, after optimizing the process parameters, we successfully fabricated a 30% HA/TCP scaffold with 30  $\mu\text{m}$  pores using this method. We then conducted shrinkage analysis and design compensation to ensure that the resulting scaffolds will precisely match the desired dimensions after post-processing. The biomimetic HA/TCP scaffolds that we fabricated using this method incorporated hierarchical features ranging from the microscale porous structure (diameter:  $\sim 20$ –1000  $\mu\text{m}$ ) to interconnected small pores ( $< 5 \mu\text{m}$ ) induced by polymer burnout during post-processing (Fig. 1b, c). The biological performance of the 3D-printed HA/TCP scaffolds was also studied. Based on our evaluation of cell proliferation, the scaffolds were biocompatible and nontoxic, providing a suitable cell culture environment. Scaffolds of 30% HA/TCP were designed and implanted into a femoral critical defect in mice along with autologous cranial neural crest cells (CNCCs) and bone marrow mesenchymal stem cells (BMMSCs). The result demonstrated that our newly developed 3D-printing method could represent a major

advancement in the fabrication of HA/TCP scaffolds for bone regeneration.

## Slurry-based $\mu$ MIP-SL

To achieve high-resolution fabrication of HA/TCP scaffolds with hierarchical structures, we developed a microscale 3D printing process based on the MIP-SL technology (Fig. 2a). In our slurry-based  $\mu$ MIP-SL, the light is reflected by a digital micro-mirror device (DMD), which has millions of integrated micro-mirrors (Texas Instruments, Inc.). The light intensity can be altered by tuning the angle of each mirror over time [38–45]. To achieve a uniform light distribution, the light is collimated by an achromatic doublet lens (Thorlabs, Inc.), and the collimated parallel light is later focused by a 4 $\times$  objective lens (Thorlabs, Inc.). The resolution of the projection image was 2.5  $\mu\text{m}/\text{pixel}$  in our slurry-based  $\mu$ MIP-SL system (Fig. 2b). To decrease distortion, a filter lens (Thorlabs, Inc.) was used to transmit light at a wavelength of 405 nm, while rejecting other wavelengths. A light monitor system, consisting of a camera, a convex lens, and a beam splitter, was also designed to monitor the projection light during the 3D printing process (Fig. 2d) [42, 43]. We

began the fabrication process by creating a computer-aided design (CAD) model to guide the manufacturing of the green part. A slurry-based  $\mu$ MIP-SL process was used to selectively cure HA/TCP suspension into complex shapes with hierarchical porous structures. In the slurry-based  $\mu$ MIP-SL process, thin layers of HA/TCP suspension are cured after sufficient exposure to a focused light beam controlled by high-resolution projection images. Accordingly, the CAD model of the 3D scaffold is sliced into a set of mask projection images, with the thickness of each layer being less than the cure depth of the HA/TCP suspension (Fig. 2c) [45]. Furthermore, in order to achieve uniform light intensity, the grayscale level of each pixel in the projection image needs to be adjusted based on a light intensity calibration database [43–45].

## Material refilling of HA/TCP slurry

The newly cured material is attached to a platform, and the bottom surface of the cured part is parallel to the surface of a glass plate coated with Teflon film. As the platform rises, a gap between the platform and the glass plate is generated, and liquid resin or slurry can flow into it if the viscosity is low enough. Driven by air pressure and self-gravity,

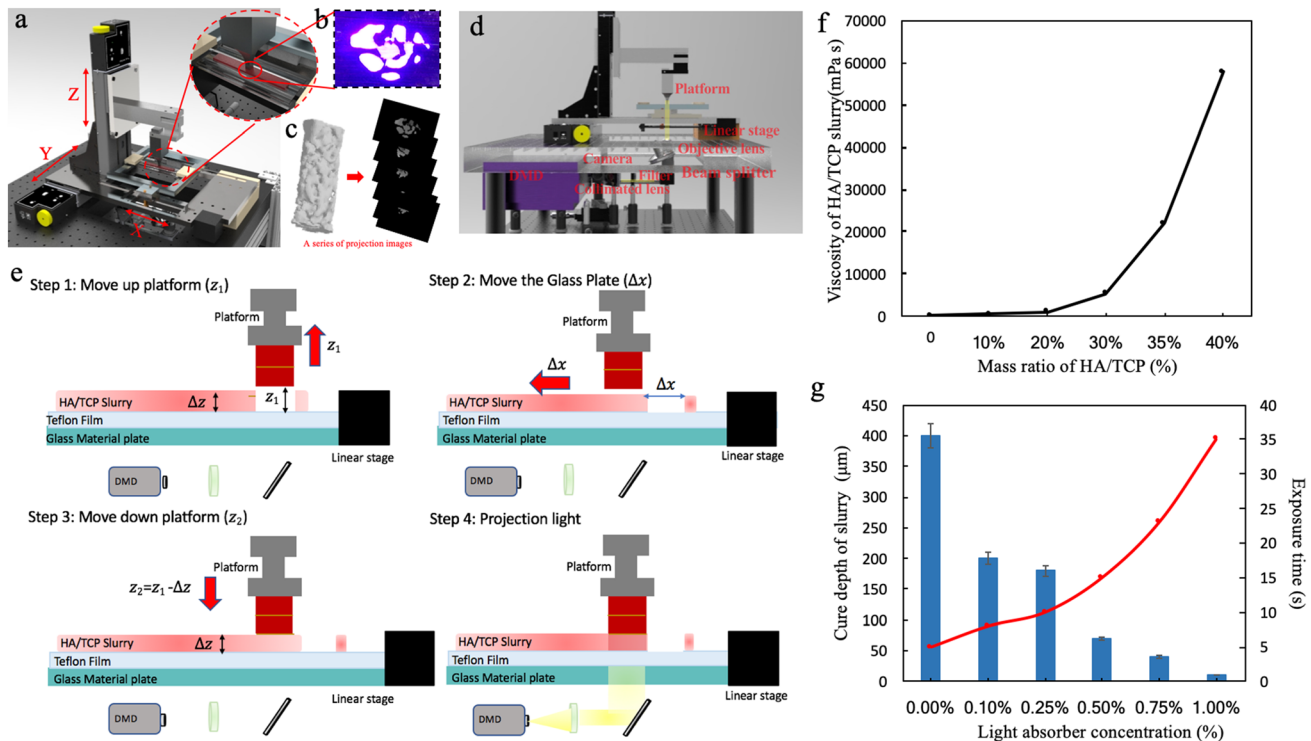


**Fig. 2** Fabrication of HA/TCP scaffold using the slurry-based  $\mu$ MIP-SL. **a** The prototype machine of slurry-based  $\mu$ MIP-SL; **b** 2D-patterned curing light beam; **c** biomimetic scaffold designed to fit mouse long bone defect was sliced into a series of projection images; **d** the optical system of the slurry-based  $\mu$ MIP-SL system; **e** the slurry

feeding process for the fabrication of highly viscous HA/TCP suspension; **f** the viscosity of HA/TCP suspension with different concentrations of HA/TCP particles; and **g** the exposure times and the cure depth for HA/TCP suspensions with different concentrations of light absorber

photocurable material flows back to refill the projection area. Since the material is incompressible liquid and its viscosity is not subject to change during the filling process, the self-filling material satisfies the Navier–Stokes momentum equation [50]:

$$v = -\frac{\Delta P}{\mu L} \left[ \left( \frac{h}{2} \right)^2 - \left( z - \frac{h}{2} \right)^2 \right] \quad (1)$$

where  $\Delta P$ ,  $v$ , and  $\mu$  represent the local pressure, velocity, and viscosity of the material, respectively,  $Z$  is the distance in the perpendicular direction, and  $h$  is the fabrication thickness of a new layer.

Based on Eq. 1, the refilling speed  $v$  of the material depends on its viscosity  $\mu$  and pressure  $P$ . The viscosity of HA/TCP suspension exponentially grows with an increase in HA/TCP concentration (Fig. 2f). When the concentration of HA/TCP particles is less than 25 wt%, the HA/TCP suspension is able to refill the fabrication area during the movement of the  $Z$  platform. Therefore, a suspension of less than 25 wt% HA/TCP can be 3D printed with self-filling using the traditional layer-based SL approach, in which the platform rises by a certain distance after each layer is cured [45]. However, when the concentration of HA/TCP particles is larger than 25 wt%, the viscosity of HA/TCP suspension dramatically increases from thousands of cPa to tens of thousands of cPa. The increased viscous resistance of the HA/TCP suspension thus obstructs the material flow between the platform and the glass plate, and the slurry cannot refill the fabrication area if the flow is only driven by air pressure and self-gravity.

Due to high viscosity of the HA/TCP suspension, the resin feeding module commonly used in the liquid-based MIP-SL systems cannot be directly applied since the HA/TCP slurry cannot refill the fabrication area spontaneously after each layer is processed. To solve the slurry feeding problem, a bottom-up MIP-SL process with auxiliary circular motion using a doctor blade was developed [46, 48, 49]. In our prototype system, the projected light from the bottom of the glass slide was focused at the top surface of the glass plate, which was coated with a Teflon film (Fig. 2d). The HA/TCP suspension was cured on the platform after receiving enough energy from the controlled light exposure. The platform was mounted on the linear stage (AeroTEC, Inc.) in the  $Z$  direction with linear motion accuracy of  $\pm 1 \mu\text{m}$ . The glass plate was fixed on a linear stage traversing along the  $X$  direction with a fast feeding speed for material refilling. A doctor blade was used to recoat the slurry on the glass plate during its linear movement in the  $X$  direction. First, a thin layer of HA/TCP suspension with a thickness of  $100 \mu\text{m}$  is evenly recoated on the top surface of the glass plate using a doctor blade (Fig. 2e). After curing one layer of HA/TCP suspension, the platform is raised by a distance greater than

the thickness of the recoated HA/TCP layer; meanwhile, the glass plate coated with HA/TCP suspension is moved in the  $X$  direction (Fig. 2e). Note the relative positions of the projection light and the building platform remain unchanged. After the glass plate's movement in the  $X$  direction, a fresh layer of recoated HA/TCP suspension is transported to the location of light projection. The platform is then slowly moved down until the distance between the already-cured surface and the glass plate is equal to the layer thickness that has been calculated based on the cure depth of the slurry. Note that the resulting layer in the 3D printing process is thinner than the layer of slurry recoated by the doctor blade and can be accurately controlled by the  $Z$  stage [49]. With the aforementioned circular movement, a new layer of HA/TCP suspension is fed to the location right below the platform within several seconds. During the building process, the circular movement is repeated until all the layers of the green part have been built on the platform.

### Curing performance of HA/TCP slurry

In order to create photocurable slurry for 3D printing, HA/TCP powders were mixed with photocurable polymer, which consists of monomers, oligomers, stabilizers, and photoinitiators. The resulting slurry can be solidified by the exposure to electromagnetic radiation [50, 51]. Since the HA/TCP suspension was solidified layer by layer to form a 3D shape, the resolution of the curing process in the  $Z$  direction was determined by the curing depth ( $C_d$ ), i.e., the distance that light could penetrate into the HA/TCP suspension and solidify the material. Compared to pure polymer, the additional HA/TCP particles absorbed and scattered light inside the HA/TCP suspension. Hence, the photosensitivity of HA/TCP suspension was reduced with the increasing concentration of HA/TCP particles. Based on the Jacobs and Griffith model [51, 52], the cure depth of the HA/TCP suspension can be quantitatively represented by the following equation:

$$C_d = k \frac{d}{\tilde{q}} \left( \frac{n_r}{n_p - n_r} \right)^2 \ln \left( \frac{E}{E_c} \right) \quad (2)$$

where  $k$  is a constant,  $d$  is the average particle size of HA/TCP,  $\tilde{q}$  is the scattering efficient value,  $n_r$  and  $n_p$  are the refractive indexes of pure resin and HA/TCP slurry, respectively,  $E$  is the projection light energy, and  $E_c$  is the critical energy required for the polymerization of material.

Although the HA/TCP powders partially blocked light, the penetration depth of the HA/TCP suspension, however, was still too large for microscale fabrication. Projection light not only solidified the top layer of HA/TCP suspension in the  $Z$  direction, but also generated unexpected curing features in the previous layers. A large  $C_d$  value created difficulty in the fabrication of micro-pores with dimensions smaller than

100  $\mu\text{m}$  in the Z direction. To reduce the light penetration depth of HA/TCP suspension, different percentages of light absorber were added into 30% HA/TCP suspension, and the cure depth of each group is shown in Fig. 2g. According to Bear's law, the light penetration depth of photocurable material is inversely proportional to the percentage  $P_d$  of light absorber [43, 44, 50]. After adding 1 wt% light absorber, the cure depth of 30wt % HA/TCP suspension was reduced from 400  $\mu\text{m}$  to only 20  $\mu\text{m}$ . The cure depth  $C_d$  of HA/TCP suspension with light absorber can be represented by the following equation:

$$C_d = k' \frac{d}{P_d \tilde{q}} \left( \frac{n_r}{n_p - n_r} \right)^2 \ln \left( \frac{E}{E_c} \right) \quad (3)$$

The exposure time  $t$  rises along with an increase in light absorber concentration. Since the projection light energy  $E$  is the product of exposure time  $t$  and light intensity, the exposure time  $t$  can be represented as:

$$t = \left( \frac{E_c}{I} \right) \exp \left( \frac{C_d P_d \tilde{q} (n_p - n_r)^2}{k' d n_r^2} \right) \quad (4)$$

The exposure time increases exponentially with an increase in light absorber concentration (refer to Fig. 2g). It only takes 5 s to cure one layer of pure 30 wt% HA/TCP suspension, while it requires 35 s to cure one layer of 30 wt% HA/TCP with 1 wt% light absorber.

## Materials and methods

### Synthesis of curable HA/TCP-based ceramic slurry

The hydroxyapatite (HA) used in this study was purchased in the form of powder with particles smaller than 200 nm (Sigma-Aldrich), and the tricalcium phosphate (TCP) was

purchased as powder with particles smaller than 4  $\mu\text{m}$  (Sigma-Aldrich). The photocurable liquid polymer resin SI500 (purchased from EnvisionTEC Inc) was used as the binder. To determine the optimal concentration  $\delta$  of HA/TCP particles, 10–40 wt% HA/TCP suspensions were prepared following the following procedures. First, equal proportions of HA and TCP powders were poured into the liquid SI500. The resulting HA/TCP slurry was then ball-milled at a rotational speed of 200 rpm for 40 min. After that, the HA/TCP suspension was degassed under a vacuum before fabrication. In addition, to study how to increase the cure depth of HA/TCP suspension, 0.1 wt%, 0.25 wt%, 0.5 wt%, 0.75 wt%, or 1 wt% light absorber (oil red from Sigma-Aldrich) was added to the 30 wt% HA/TCP suspension, with the rest of the preparation procedure identical.

### Post-processing of 3D-printed scaffold

After the green part was printed using the slurry-based  $\mu\text{MIP-SL}$  process, post-processing procedures consisting of debinding at a low temperature and sintering at a high temperature were used to entirely remove the polymer in the scaffold, and to fuse the HA/TCP particles together (Fig. 3). The temperature settings during the debinding process followed the curve shown in Fig. 3a. A tube furnace (GSL-1100X-SK purchased from MTI Corp) was used in the debinding process. The generated gas was continuously exhausted by a vacuum pump to maintain the pressure of the heating zone at  $-0.1$  mPa. Note that the rate of heating during the debinding process should be slow to ensure the decomposition rate of the polymer is slower than the pyrolysis rate. Otherwise, the green part may be damaged by the gas generated by the pyrolysis process. In our study, the heating rate was set to 1  $^{\circ}\text{C}/\text{min}$ . In addition, the temperature was held for 30 min at every increment of 100  $^{\circ}\text{C}$  until the temperature reached 600  $^{\circ}\text{C}$ . The temperature was then maintained at 600  $^{\circ}\text{C}$  for 180 min to ensure the polymer was fully removed [48].

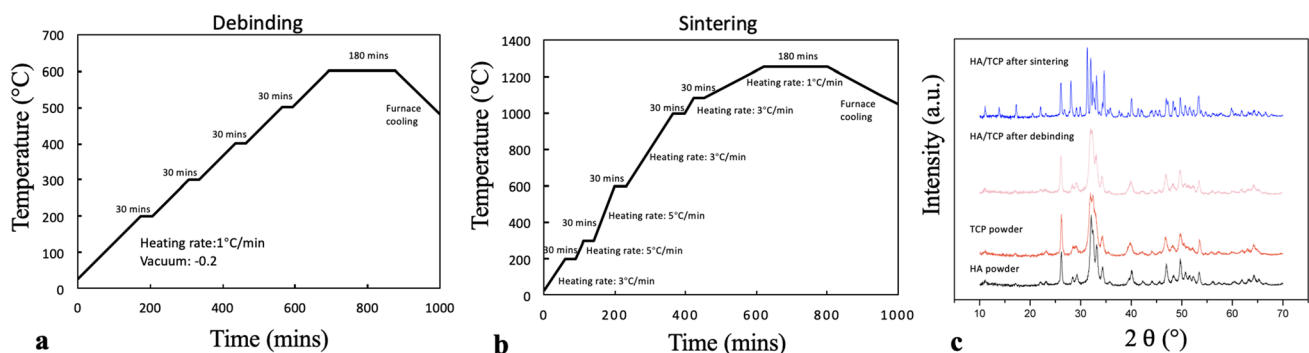


**Fig. 3** Post-processing of 3D-printed HA/TCP scaffolds. **a** The temperature curve of the debinding process; **b** the temperature curve of the high-temperature sintering process; and **c** the X-ray diffraction of 30% HA/TCP scaffold before and after the debinding and sintering processes

During the debinding process, pores form in places where polymer burns out. Since the HA/TCP particles are then sparsely arranged, the brown part has insufficient strength to support external loads. Therefore, an additional sintering process is necessary in order to fuse the HA/TCP particles together to further improve the mechanical properties of the scaffold. The shrinkage ratio and mechanical strength of the scaffold are determined by the sintering temperature, as it has an influence on the grain boundary and volume diffusion of the ceramic particles [50, 53, 54]. Three different sintering temperatures (1050 °C, 1150 °C, and 1250 °C) were tested to identify the optimum. A GSL-1500 furnace (MTI Corp.) was used to sinter the HA/TCP brown parts in normal air conditions. The temperature curve for the 1250 °C sintering process is shown in Fig. 3b. Specifically, the temperature was gradually increased to 1080 °C and held there for 30 min. Afterward, the sample was heated to 1250 °C and maintained at that temperature for 180 min. Finally, samples were allowed to cool to room temperature before removing them. For the sintering process at 1050 °C, the temperature was increased and maintained at 1050 °C for 180 min with similar heating rates as the ones shown for 1250 °C.

## Characterization of 3D-printed scaffold

### XRD testing

To verify the changes to the composition, structure, and physical properties of HA/TCP scaffold after the debinding and sintering processes, the scaffolds were characterized using X-ray diffraction (XRD) after each step. The comparison of the original HA/TCP particles and the HA/TCP scaffold after each post-processing step is shown in Fig. 3c.

### Mechanical testing

Mechanical properties of the post-processed HA/TCP scaffold were studied using a compression machine (Instron 5492 dual column testing systems, Instron, MA, USA). We built 2 mm × 2 mm × 2 mm HA/TCP solid cubes for the compression tests ( $n=3$  per case) [55]. Each specimen was tested by gradually increasing the load until the sample failed completely. The compressive strength of HA/TCP material was calculated based on the stress–strain curve.

### Porosity testing

A gravimetric (Archimedes) method was applied to calculate the porosity of the final scaffold after post-processing. The scaffold mass  $M_d$  in the dry state was first measured. The HA/TCP scaffold was then immersed in silicone oil and then subjected to a vacuum to completely saturate the pores with the silicone. Following that, the mass  $M_{sat}$  of

the saturated scaffold was measured again. The scaffold was then immersed in a water tank, and the mass  $M_{sub}$  was measured. The porosity  $P$  of the scaffold was then calculated. Scaffolds fabricated with 20–40 wt% concentration of HA/TCP particles were measured using the aforementioned method. Furthermore, ImageJ software was used to calculate the porosity and its distribution of the HA/TCP scaffolds by analyzing scanning electron microscopy (SEM) images under high magnification. For each case, three samples were tested under the same conditions, and the results were averaged.

## Biocompatibility and bioactivity

NIH3T3 cells were cultured in Dulbecco's modified Eagle's medium with 10% of fetal bovine serum.  $1 \times 10^6$  cells were loaded on the surface of the gel-coated HA/TCP scaffold and incubated at 37 °C. Cell viability was observed at different time points using a live and dead staining assay following standard protocol.

$1 \times 10^4$  cells were seeded on a 96-well plate and allowed for 24 h for attachment. Scaffolds with different percentages of HA/TCP were cultured with the cells to test their effect on cell proliferation. After 48 h of co-culture, cell proliferation was measured using an MTT assay.

### Animals

Male immunocompromised mice at 8–10 weeks old (athymic nude, nu/nu, Jackson Laboratory, Sacramento, CA) were used in the present study. All mouse experiments were conducted in accordance with protocols approved by the Institutional Animal Care and Use Committee of the University of Southern California.

### Mouse dental pulp cell culture

The dental pulp mesenchyme from the mandibular incisor of P3.5 mice was separated, minced, and digested with the solution containing 2 mg/ml collagenase type I (Worthington Biochemical) and 4 mg/ml dispase II (Roche Diagnostics) in PBS for 1 h at 37 °C. A single-cell suspension was obtained by passing the cells through a 70 µm strainer (BD Biosciences) and was seeded in 10-cm plate culture dishes (Corning) with  $\alpha$ -MEM supplemented with 20% FBS, 2 mm L-glutamine, 55 µm 2-mercaptoethanol, 100 U/ml penicillin, and 100 µg/ml streptomycin (Life Science Technologies). The culture medium was changed after an initial incubation for 48 h.

## Mouse long bone defect model

In mice, long bone defect was generated by removing a piece of long bone such that the edges of the remaining bone are separated by 2 mm. To create a long bone critical-sized defect, animals were placed in ventral recumbency with the left hind limb in extension. An anterolateral approach was used to expose the anterior surface of the femur. Briefly, after a lateral longitudinal cutaneous incision along the femur extending from the hip joint to the stifle joint, the fascia lata was incised to expose the full length of the femur, preserving the sciatic nerve caudally and the articular capsule distally. An anterior polyetheretherketone (PEEK) microlocking plate (MouseFix plate; RISystem AG, Davos, Switzerland) was applied on the anterior femoral side. Next, four holes were drilled using a 0.3-mm drill bit (RISystem AG, Davos, Switzerland) through the most proximal and most distal holes of the plate and four self-tapping locking screws (Mouse-Fix screw 2 mm; RISystem AG, Davos, Switzerland) were inserted and locked to secure the plate. Gigli saws (0.22 mm; RISystem AG, Davos, Switzerland) were then inserted, one each in the two slots of the jig (Drill and Saw Guide; RISystem AG, Davos, Switzerland), and a 2-mm-long mid-diaphyseal femoral osteotomy was subsequently performed. The defect was either left empty or filled with the HA/TCP scaffolds with or without cells.

## Statistical analysis

The statistical analysis theory was applied in the experimental design and analysis in this study [56]. All data presented here were with  $\pm$  standard deviation (SD). The significance index  $*p < 0.005$  was chosen to indicate the statistical significance in the proliferation experiment [56].

## Results and discussion

### Porosity and mechanical performance

The debinding and sintering procedures are conducted after the green part has been printed using the slurry-based  $\mu$ MIP-SL process. During the debinding process, the photopolymer must be removed completely, because residual carbon has a significant impact on the following sintering process, and ultimately on the biological performance of HA/TCP scaffold. We found that as the temperature increased from 300 to 600 °C during debinding, the weight of the fabricated green part decreased dramatically. When the temperature reached 600 °C, the weight of the green part

maintained at a constant value and only HA/TCP particle and small amount of carbon were left (Fig. 4a) [48, 49].

In the debinding process, photopolymer in the green part was removed after raising the temperature to over 600 °C. Afterward, the brown part of HA/TCP scaffold is obtained [57]. At this stage, the porosity  $P$  of HA/TCP scaffold reaches its peak value. However, the brown part is fragile due to the loose arrangement of HA/TCP particles (Fig. 4a); hence, a sintering process is required to improve bonding between HA/TCP particles. As shown in the X-ray diffraction results (Fig. 4c), the scaffold after the debinding process showed similar integrated intensity to the original HA and TCP particles. However, after the sintering process, both the peak counts and the peak values of the HA/TCP scaffolds increased because the size of the HA/TCP particles was larger than those of the original HA/TCP powders. The effects of sintering temperature  $T_s$  and HA/TCP particle concentration  $\delta$  on the porosity and mechanical performance of the resulting scaffold were investigated in our study. Based on a literature review [21], three different sintering temperatures (1050 °C, 1150 °C, and 1250 °C) were tested in order to identify an appropriate sintering temperature for different concentrations of HA/TCP particles (Fig. 4a).

The porosity of an HA/TCP scaffold is determined by the particle size, the sintering temperature, and the concentration of particles [57, 58]. The porosity decreases linearly with an increase in sintering temperature (Fig. 4c). For instance, the porosity  $P$  of a 30 wt% HA/TCP scaffold is reduced by 6%, when the sintering temperature is raised from 1050 to 1250 °C. Compared to the sintering temperature, the concentration of HA/TCP particles has a more significant impact on the porosity (Fig. 4c). We analyzed the pore size distribution in our scaffolds and found that the pore size of a sintered HA/TCP scaffold is mainly in the nanoscale range (Fig. 4d). This is because an increase in the main grain size of the HA/TCP particles further reduces the space between each grain after sintering, and the grain of HA/TCP particles grows much larger at higher temperatures.

The porosity of an HA/TCP scaffold is a significant factor that affects its mechanical performance. The mechanical strength of a scaffold can be expressed as in the following equation [59]:

$$\sigma = \sigma_0 \exp(-ap) \quad (5)$$

where  $\sigma$  is the strength of the scaffold,  $\sigma_0$  is the strength of solid HA/TCP without pores, and  $a$  is a constant.

Although we found that the porosity  $P$  of a 20 wt% HA/TCP scaffold sintered at 1050 °C was the greatest among the concentrations that we tested, such a scaffold is not strong enough to support compression load from the two sides of the neighboring bone. The compressive strength of an HA/TCP scaffold can be improved by raising the sintering

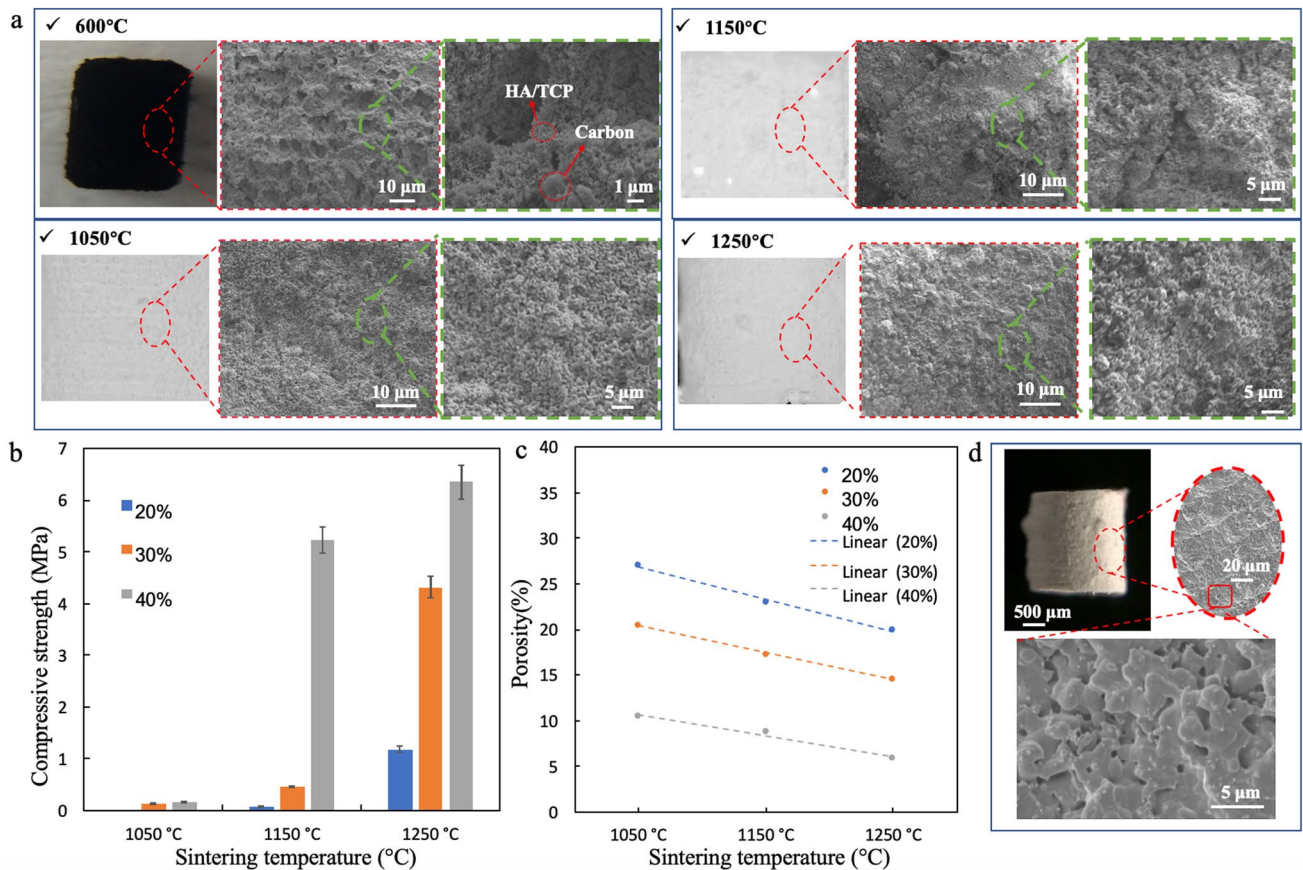


**Fig. 4** The porosity and mechanical performance of 3D-printed HA/TCP rod sintered under different conditions. **a** Optical microscopic and SEM images of 3D-printed 30 wt% HA/TCP rod after post-processing under different temperatures; **b** the compressive strength of

3D-printed HA/TCP rod fabricated under different conditions; **c** the porosity of 3D-printed HA/TCP rod fabricated under different conditions; and **d** optical microscope and SEM images of a 3D-printed 30 wt% HA/TCP rod sintered at 1250 °C

temperature  $T$  or increasing the particle concentration  $\delta$  in the HA/TCP suspension. For instance, the compressive strength of 30 wt% HA/TCP increases from 0.13 to 4.32 mPa when the sintering temperature  $T$  is raised from 1050 to 1250 °C. The compressive strength of HA/TCP sintered at 1250 °C improves by five times when the concentration  $\delta$  of HA/TCP is increased from 20 to 40 wt% (Fig. 4b). Overall, a 30 wt% HA/TCP scaffold sintered at 1250 °C showed advantages over the other tested scaffolds when considering both porosity and mechanical performance.

However, in scaffolds made from 30 wt% HA/TCP, the pores are small after sintering at 1250 °C. As shown in Fig. 4d, the average pore size for such scaffolds is smaller than 5  $\mu\text{m}$ . Even though their mechanical strength is acceptable, it is difficult for nutrients and blood vessels to pass through such a dense HA/TCP scaffold. The pore size directly correlates with the amount of nutrient and oxygen diffusion and cell integration. For this reason, the porosity of the scaffold plays an essential role in bone formation. We therefore generated two new scaffold designs with more microscale porosity, which will be discussed in “Complex

scaffold fabrication with hierarchical porous structures” section.

### Shrinkage analysis and compensation

Since photocurable polymer was removed and HA/TCP particles were sintered together in post-processing, the total volume of a sintered HA/TCP scaffold was reduced from that of the green part fabricated by the  $\mu\text{MIP-SL}$  process (Fig. 5a). As shown in Fig. 5b, the shrinkage in the Z direction ( $r_{sz}$ ) and in the XY plane ( $r_{sr}$ ) can be calculated as follows:

$$\begin{cases} r_{sz} = \frac{H-H_s}{H} \\ r_{sr} = \frac{D-D_s}{D} \end{cases} \quad (6)$$

The shrinkage ratio  $r_s$  is closely related to the concentration of HA/TCP particles  $\delta$  and the sintering temperature  $T$  [50, 60]. The shrinkage ratio  $r_s$  of an HA/TCP scaffold increases as the concentration of HA/TCP particles decreases, since the more internal polymer is burned off (Fig. 5c). Hence, as the concentration of HA/TCP particles

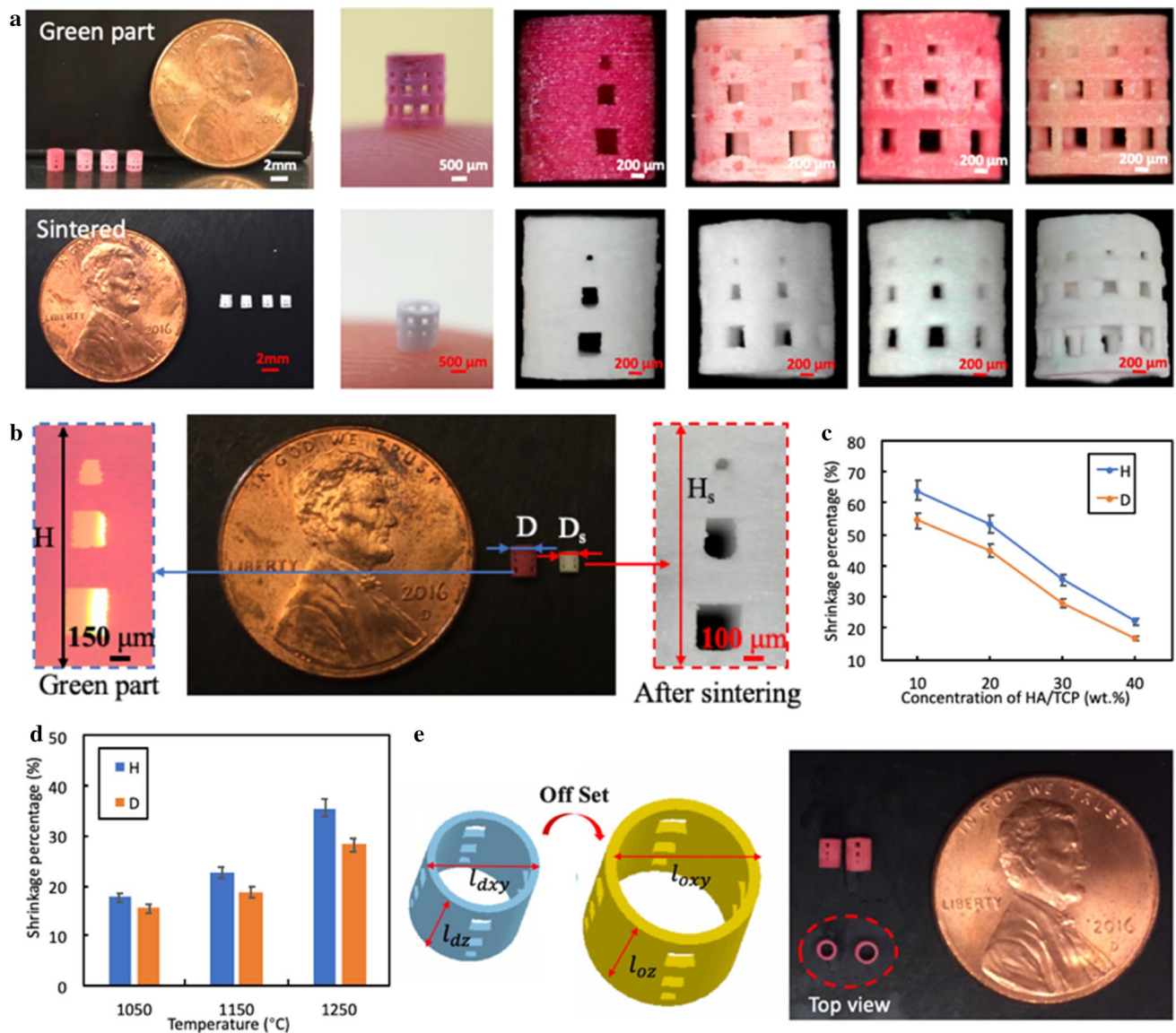


**Fig. 5** The shrinkage of an HA/TCP scaffold after sintering. **a** Microscopic image of 3D-printed 30 wt% HA/TCP before and after post-processing; **b** shrinkage ratios of 30 wt% HA/TCP scaffolds in the Z and XY directions under different sintering conditions; **c** shrinkage ratios of HA/TCP scaffolds with different concentrations of HA/TCP

particles on height (Z direction) and diameter (XY direction); **d** the offset operation for shrinkage compensation; and **e** the offset operation for shrinkage compensation and 3D-printed HA/TCP scaffolds before and after incorporating shrinkage compensation

increases from 10 to 40 wt%, the axial shrinkage ratio  $r_{sz}$  of an HA/TCP scaffold sintered at 1150 °C declines from 45.25 to 17.8%. The same tendency can be observed when the sintering temperature  $T$  is increased (Fig. 5d). This happens as diffusion increases with the increase in sintering temperature, and the HA/TCP particles become closer to each other [61, 62]. For example, 30 wt% HA/TCP scaffold sintered at 1050 °C shrinks only 17.75% in the axial (Z) direction, but shrinks by 35.5% when the sintering temperature is increased to 1250 °C.

The shrinkage ratio  $r_s$  of an HA/TCP scaffold is also affected by the geometric design. We fabricated 30 wt% HA/TCP scaffolds with different densities of microholes (12, 18, 24, and 30 pores per scaffold), with each of the pores designed within 200  $\mu\text{m}$  to 400  $\mu\text{m}$  edge lengths (Fig. 5a). The volumetric shrinkage of an HA/TCP scaffold is less when the scaffold is designed with a higher density of microholes. Furthermore, the shrinkage ratio  $r_s$  of an HA/TCP scaffold can vary in both the axial (Z) and radial (XY) directions. As shown in Fig. 5a, b, the shrinkage ratio  $r_{sz}$  in

the axial direction is greater than the shrinkage ratio  $r_{sz}$  in the radial direction. Specifically, an HA/TCP scaffold made from a 30 wt% HA/TCP suspension reduces from 2 mm to only 1.29 mm in the axial direction after being sintered at 1250 °C, while the diameter of the scaffold shrinks from 1.8 to 1.29 mm. This is because the HA/TCP suspension is uniformly solidified under the light exposure in the *XY* direction; hence, the stress is more isotropic in the radial plane. In contrast, the HA/TCP suspension is stacked layer by layer in the *Z* direction; hence, the stress in the *Z* direction is not identical to that in the *XY* plane. Thus, the 3D-printed HA/TCP scaffold shows anisotropic shrinkage behaviors.

HA/TCP scaffolds shrink in both the axial and radial directions after the sintering process. To achieve accurate shape control in the fabrication of HA/TCP scaffolds with microscale pores, a dimensional offset needs to be applied to the input CAD model to compensate for the dimensional shrinkage [63, 64]. The compensation factor  $\theta_z$  was investigated according to the shape-changing rate of the microsquares in the *Z* direction. The dimensions of hierarchical microscale features were adjusted according to the

compensations required in the axial and radial directions, based on the formulas as follows:

$$\begin{cases} l_{dxy} = \theta_{xy} l_{oxy} \\ l_{dz} = \theta_z l_{oz} \end{cases} \quad (7)$$

where  $l_{dxy}$  and  $l_{dz}$  are printing dimensions of microstructures in the axial and radial directions, respectively;  $l_{oxy}$  and  $l_{oz}$  are the ideal dimensions in the axial and radial directions, respectively; and  $\theta_{xy}$  and  $\theta_z$  are two constants, which were empirically determined to be 1.39 and 1.55 for 30 wt% HA/TCP scaffold sintered at 1250 °C.

### Complex scaffold fabrication with hierarchical porous structures

To test the printing capability of the developed  $\mu$ MIP-SL process in the *X/Y* plane and in the *Z* direction, two groups of 2 mm cylindrical shells were designed as follows. To examine the fabrication precision in the *X/Y* plane, rectangular pores with a height of 200  $\mu$ m and width ranging

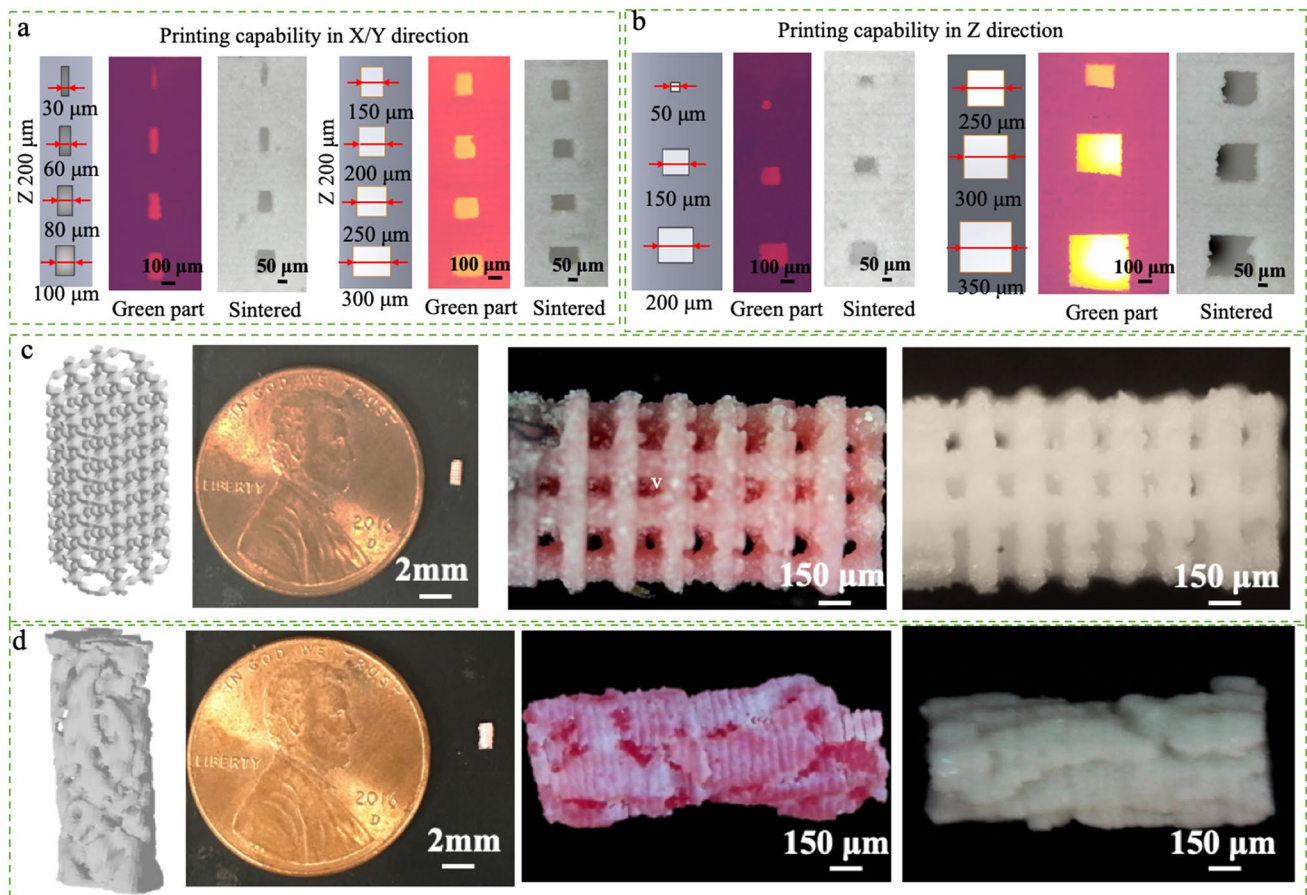


**Fig. 6** HA/TCP scaffolds with hierarchical porous structures. **a** The printing capability of the developed slurry-based  $\mu$ MIP-SL in the *XY* direction; **b** the printing capability of the developed slurry-based

$\mu$ MIP-SL in the *Z* direction; and the CAD model and fabrication results of HA/TCP scaffolds with **c** micro-lattice and **d** biomimetic bone structures

from 30  $\mu\text{m}$  to 300  $\mu\text{m}$  were designed on the side wall of the scaffold, which was 250  $\mu\text{m}$  in thickness (Fig. 6a). To examine the fabrication capability in the Z direction, another scaffold with square pores was designed, with pore heights ranging from 50 to 350  $\mu\text{m}$  (Fig. 6b). The printing accuracy of the HA/TCP scaffolds was investigated by comparing the original design size with the final printing size of scaffolds. The fabrication error of HA/TCP scaffold printed by using our slurry-based  $\mu\text{MIP-SL}$  is  $\pm 5 \mu\text{m}$ .

Natural bone has hierarchical porous structures with dimensions ranging from hundreds of microns to a few nanometers [1]. Because we are able to compensate for fabrication shrinkage in the design phase, our process can accurately fabricate porous structures with holes ranging from hundreds to tens of microns. In addition, the post-processing procedures can create holes in the fabricated porous structures ranging from a few microns to nanometers. In this study, both micro-lattice structure and biomimetic bone structure were designed and fabricated using the slurry-based  $\mu\text{MIP-SL}$  process that we developed. We designed HA/TCP scaffolds with hierarchical structures for the regeneration of bone matrix based on a digital CT scan of a mouse femur. To increase their compressive stress, scaffolds of 2 mm in height and 0.9 mm in diameter with micro-lattice and biomimetic bone structures were designed for use in vivo as described below. Unlike the mesh structure, scaffolds with the lattice and biomimetic structures require a much more complicated design approach [65]. The basic unit cells of micro-lattice and biomimetic structures were firstly designed, respectively; we then repeatedly perform Boolean operations of unit cells to form a periodic structure. After that, we intersect it with the desired long bone defect shape to create the final scaffold with micro-lattice and biomimetic bone structures. The scaffolds with lattice structures incorporated microscale pores ranging from 50  $\mu\text{m}$  to 150  $\mu\text{m}$  in diameter. The biomimetic bone structure scaffolds had microscale porous structures ranging from 60 to 100  $\mu\text{m}$ . The CAD models and 3D-printed HA/TCP scaffolds with micro-lattice structures and biomimetic bone structures are shown in Fig. 5c, d, respectively. The compressive strengths of the HA/TCP scaffolds designed with biomimetic bone structure and with microscale lattice structure were 9.5 MPa and 15.5 MPa, respectively, which could provide satisfactory mechanical performance for bone engineering applications. Moreover, the porosities of both structural designs were greatly improved as hundreds of micro-pores were added in the design and successfully fabricated using our developed 3D printing process. These pores, similar to those in natural bones, are important for cell growth within the scaffold.

## Biocompatibility and bioactivity of 3D-printed scaffold

The biocompatibility of the 3D-printed HA/TCP scaffolds was tested. Specifically, we first tested the viability of cells cultured on the surfaces of scaffolds with micro-lattice structures. Within 24 h after seeding, cells were able to attach to the scaffolds and showed normal spindle shape, suggesting a healthy condition. We further performed live and dead staining at different time points after seeding. After 24 h, we were barely able to detect any dead cells. After 96 h, we observed a slight increase in dead cells. The percentage of dead cell after 24 h and 96 h was calculated, respectively. For the quantification of dead/live cells, pictures were chosen at three places randomly, and the number of live cells (green) and dead cells (red) was counted using ImageJ. The result is shown in Fig. 7a, and the dead cells were still less than 10% of the total cell population. We also investigated the effects of scaffolds fabricated with different concentrations of HA/TCP particles on cell proliferation (Fig. 7b). After 3 days, cells cultured with HA/TCP scaffolds showed similar growth rates to the control group cultured without scaffolds. We did not observe any significant difference between the groups cultured with scaffolds of different HA/TCP concentrations. Collectively, these data clearly suggest that the HA/TCP-based scaffolds produced using our 3D printing method are biocompatible.

After establishing biocompatibility in vitro, we tested stem cell-mediated bone regeneration with the HA/TCP scaffolds. The mouse femur represents an excellent defect model for bone regeneration because of the fact that it is load bearing, its manner of ossification, and its relative lack of influence from the surrounding microenvironment. However, this model presents significant difficulties for the scaffold fabrication due to the small size of the animal. To test the capacity of our scaffolds to support bone regeneration, we used a surgical technique to generate a femoral defect in live nude mice (Fig. 7c–f). Previous studies have shown that CNCCs are more robust in proliferation and produce more cortical bone when implanted in calvarial injury sites, whereas BMMSCs produce more bone marrow, suggesting that the organization and relative amounts of these components will affect the quality of new bone created with tissue engineering [66, 67]. About one million bone marrow-derived mesenchymal stem cells (BMMSCs) and cranial neural crest cells (CNCCs) were loaded onto 3D-printed HA/TCP scaffolds. Both thin-shell-shaped and biomimetic-bone-structure-shaped scaffolds were implanted into a femoral defect in live nude mice. The mechanical performance of scaffolds can meet the requirement of experiment, and the scaffold maintained the shape during the surgery. Meanwhile, an additional group of mice received the same amount of stem cells, but no scaffold. The bone regeneration

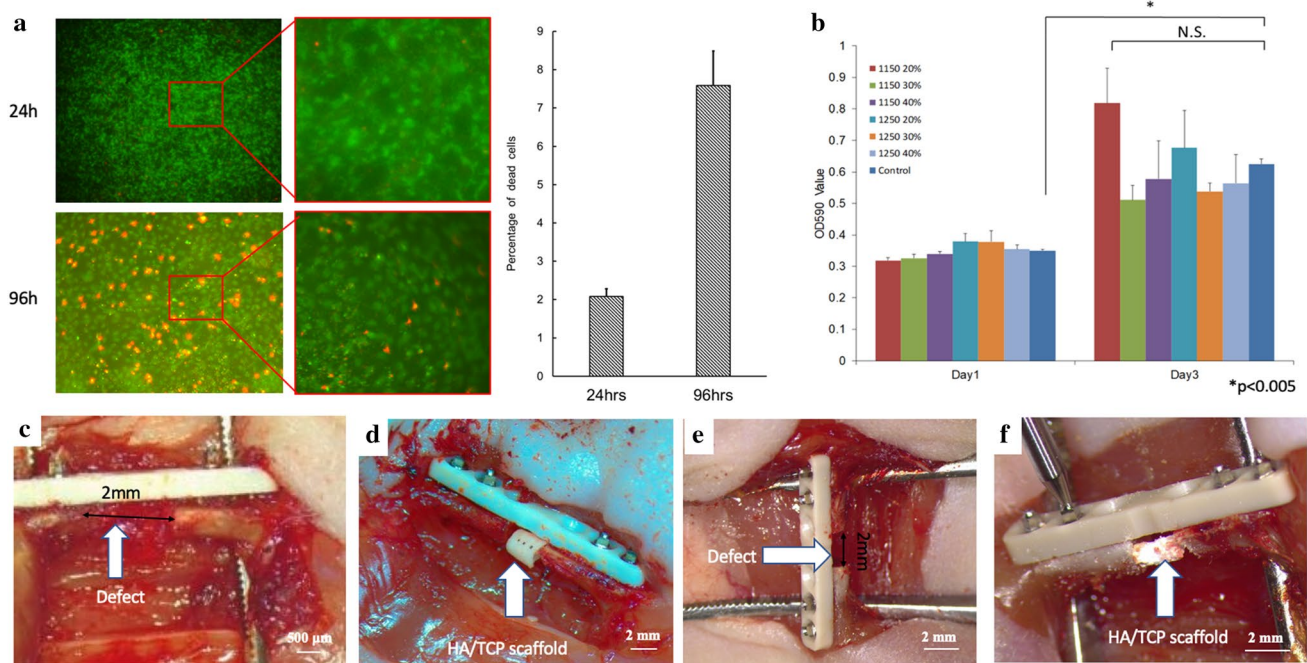


**Fig. 7** Biocompatibility of HA/TCP scaffolds printed under different conditions and live nude mice animal implant with printed scaffold. **a** Cell viability of HA/TCP scaffold, with dead cells indicated by red fluorescence. Red boxed regions appear under higher magnification at right. The percentage of dead cell was quantified; **b** statistics for the proliferation of cells cultured with HA/TCP scaffolds printed with various concentrations of HA/TCP (\* $p < 0.05$  indicated there was a

significant difference between different days); **c** the 2 mm defect and PEEK plate used to stabilize the limb; **d** thin-shell-shaped HA/TCP scaffold implanted with BMMSCs and CNCCs in the defect; **e** the 2 mm defect and PEEK plate used to stabilize the limb; and **f** bone-shaped HA/TCP scaffold implanted with BMMSCs and CNCCs in the defect

of defect with and without scaffold is still under study, and we will analyze the bone growth data in the future.

## Conclusions

Material composition and functional structure are two essential factors to consider when developing scaffolds for applications in tissue engineering and regenerative medicine. The biocompatible ceramic HA/TCP is widely used in bone regeneration because it provides superior performance relative to other materials by promoting the adhesion and proliferation of bone-forming cells. However, it is difficult to form complex geometric shapes from HA/TCP using current manufacturing methods. In this paper, we presented a slurry-based  $\mu$ MIP-SL process, which made it possible to use nanoscale HA/TCP particles to build HA/TCP scaffolds with complex hierarchical porous structures. First, the curing performance of HA/TCP suspension was studied, and our 3D printing method, which features a novel slurry feeding module, was introduced and demonstrated. The post-processing settings and suspension constituents used for fabricating HA/TCP scaffolds by this method were systematically optimized to achieve the desired structural

porosity and mechanical properties. To improve the fabrication accuracy of hierarchical porous structures, a shape compensation scheme was developed based on the shrinkage behavior of HA/TCP during the fabrication process. To achieve high mechanical strength with sufficient porosity, HA/TCP scaffolds with biomimetic bone structure and micro-lattice structure were designed and fabricated. Both biocompatibility and bioactivity tests were conducted, and the results demonstrated that the HA/TCP scaffold is biocompatible. The strength of the HA/TCP scaffold was tested, and the results showed that HA/TCP scaffold has sufficient mechanical strength for the surgery in a nude mouse in vivo model of the long bone with cranial neural crest cells and bone marrow mesenchymal stem cells. In the future, bone regeneration will be observed and analyzed. Furthermore, nanoscale HA/TCP particles combined with other biodegradable polymers will be fabricated using the 3D printing method described here to speed up the degradation of the scaffolds, and other bio-molecules such as growth factors will be integrated into the scaffolds to further accelerate bone healing.

**Acknowledgements** The work was supported by the Alfred E. Mann Institute at University of Southern California as a grant to Yang Chai

and Yong Chen. The authors also acknowledge the support of National Science Foundation (NSF) grants 1151191 and 1335476 and the Core Center of Excellence in Nano Imaging (CNI) at USC for the use of microscopic measuring equipment.

## Compliance with ethical standards

**Conflict of interest** The authors declare there is no conflict of interest.

**Ethical approval** The animal experiments in this study were approved by the Institutional Animal Care and Use Committee of the University of Southern California. All applicable guidelines and protocols for care and use of animals were followed.

## References

- Basu B (2017) Natural bone and tooth: structure and properties. In: Basu B, Ghosh S (eds) *Biomaterials for musculoskeletal regeneration*. Springer, Singapore, pp 45–85
- Wang Q et al (2017) Artificial periosteum in bone defect repair—a review. *Chin Chem Lett* 28(9):1801–1807
- Yu JC et al (1996) An experimental study of the effects of craniofacial growth on the long-term positional stability of microfixation. *J Craniofacial Surg* 7(1):64–68
- Stelnicki EJ, Hoffman W (1998) Intracranial migration of microplates versus wires in neonatal pigs after frontal advancement. *J Craniofacial Surg* 9(1):60–64
- Macchetta A, Turner IG, Bowen CR (2009) Fabrication of HA/TCP scaffolds with a graded and porous structure using a camphene-based freeze-casting method. *Acta Biomater* 5(4):1319–1327
- Miao X et al (2008) Mechanical and biological properties of hydroxyapatite/tricalcium phosphate scaffolds coated with poly (lactic-co-glycolic acid). *Acta Biomater* 4(3):638–645
- Ho CMB, Ng SH, Yoon Y-J (2015) A review on 3D printed bioimplants. *Int J Precis Eng Manuf* 16(5):1035–1046
- Bose S, Vahabzadeh S, Bandyopadhyay A (2013) Bone tissue engineering using 3D printing. *Mater Today* 16(12):496–504
- Rengier F et al (2010) 3D printing based on imaging data: review of medical applications. *Int J Comput Assist Radiol Surg* 5(4):335–341
- Kim S-S et al (2006) Poly (lactide-co-glycolide)/hydroxyapatite composite scaffolds for bone tissue engineering. *Biomaterials* 27(8):1399–1409
- Sato M et al (2006) Increased osteoblast functions on undoped and yttrium-doped nanocrystalline hydroxyapatite coatings on titanium. *Biomaterials* 27(11):2358–2369
- Shao H et al (2017) Bone regeneration in 3D printing bioactive ceramic scaffolds with improved tissue/material interface pore architecture in thin-wall bone defect. *Biofabrication* 9(2):025003
- Xu S et al (2017) Effects of HAp and TCP in constructing tissue engineering scaffolds for bone repair. *J Mater Chem B* 5(30):6110–6118
- Cao H, Kuboyama N (2010) A biodegradable porous composite scaffold of PGA/β-TCP for bone tissue engineering. *Bone* 46(2):386–395
- Rakovsky A et al (2014) β-TCP-poly(lactide) composite scaffolds with high strength and enhanced permeability prepared by a modified salt leaching method. *J Mech Behav Biomed Mater* 32:89–98
- Nakahira A et al (2005) Fabrication of porous hydroxyapatite using hydrothermal hot pressing and post-sintering. *J Am Ceram Soc* 88(5):1334–1336
- Zhou S et al (2011) Fabrication of hydroxyapatite/ethylene-vinyl acetate/polyamide 66 composite scaffolds by the injection-molding method. *Polym Plast Technol Eng* 50(10):1047–1054
- Bose S et al (2003) Pore size and pore volume effects on alumina and TCP ceramic scaffolds. *Mater Sci Eng, C* 23(4):479–486
- Tarafder S et al (2015) SrO- and MgO-doped microwave sintered 3D printed tricalcium phosphate scaffolds: mechanical properties and in vivo osteogenesis in a rabbit model. *J Biomed Mater Res Part B Appl Biomater* 103(3):679–690
- Tarafder S et al (2013) Microwave-sintered 3D printed tricalcium phosphate scaffolds for bone tissue engineering. *J Tissue Eng Regen Med* 7(8):631–641
- Zeng Y et al (2018) 3D printing of hydroxyapatite scaffolds with good mechanical and biocompatible properties by digital light processing. *J Mater Sci* 53(9):6291–6301
- Huang W et al (2013) Fabrication of HA/β-TCP scaffolds based on micro-syringe extrusion system. *Rapid Prototyp J* 19(5):319–326
- Nyberg E et al (2017) Comparison of 3D-printed poly-ε-caprolactone scaffolds functionalized with tricalcium phosphate, hydroxyapatite, bio-oss, or decellularized bone matrix. *Tissue Eng Part A* 23(11–12):503–514
- Leukers B et al (2005) Hydroxyapatite scaffolds for bone tissue engineering made by 3D printing. *J Mater Sci Mater Med* 16(12):1121–1124
- Cox SC et al (2015) 3D printing of porous hydroxyapatite scaffolds intended for use in bone tissue engineering applications. *Mater Sci Eng, C* 47:237–247
- Wu C et al (2015) Graphene-oxide-modified β-tricalcium phosphate bioceramics stimulate in vitro and in vivo osteogenesis. *Carbon* 93:116–129
- Kon E et al (2000) Autologous bone marrow stromal cells loaded onto porous hydroxyapatite ceramic accelerate bone repair in critical-size defects of sheep long bones. *J Biomed Mater Res* 49(3):328–337
- Kim J et al (2012) Rapid-prototyped PLGA/β-TCP/hydroxyapatite nanocomposite scaffolds in a rabbit femoral defect model. *Biofabrication* 4(2):025003
- Witek L (2015) Extrusion-based, three-dimensional printing of calcium-phosphate scaffolds. Dissertation of Oklahoma State University
- Diogo GS et al (2014) Manufacture of β-TCP/alginate scaffolds through a Fab@ home model for application in bone tissue engineering. *Biofabrication* 6(2):025001
- He F et al (2017) Fabrication of β-tricalcium phosphate composite ceramic sphere-based scaffolds with hierarchical pore structure for bone regeneration. *Biofabrication* 9(2):025005
- Castilho M et al (2014) Direct 3D powder printing of biphasic calcium phosphate scaffolds for substitution of complex bone defects. *Biofabrication* 6(1):015006
- Zhang Y et al (2017) 3D-printed bioceramic scaffolds with antibacterial and osteogenic activity. *Biofabrication* 9(2):025037
- Trombetta R et al (2017) 3D printing of calcium phosphate ceramics for bone tissue engineering and drug delivery. *Ann Biomed Eng* 45(1):23–44
- Castilho M et al (2015) Fabrication of individual alginate-TCP scaffolds for bone tissue engineering by means of powder printing. *Biofabrication* 7(1):015004
- Nadeem D et al (2015) Three-dimensional CaP/gelatin lattice scaffolds with integrated osteoinductive surface topographies for bone tissue engineering. *Biofabrication* 7(1):015005
- Di Luca A et al (2016) Toward mimicking the bone structure: design of novel hierarchical scaffolds with a tailored radial porosity gradient. *Biofabrication* 8(4):045007
- Yang Y et al (2018) Recent progress in biomimetic additive manufacturing technology: from materials to functional structures. *Adv Mater* 30(36):1706539

39. Holmes B et al (2016) A synergistic approach to the design, fabrication and evaluation of 3D printed micro and nano featured scaffolds for vascularized bone tissue repair. *Nanotechnology* 27(6):064001
40. Salerno A et al (2017) Synthetic scaffolds with full pore interconnectivity for bone regeneration prepared by supercritical foaming using advanced biofunctional plasticizers. *Biofabrication* 9(3):035002
41. Yang J-Z et al (2015) Structure design and manufacturing of layered bioceramic scaffolds for load-bearing bone reconstruction. *Biomed Mater* 10(4):045006
42. Yang Y et al (2018) 3D-printed biomimetic super-hydrophobic structure for microdroplet manipulation and oil/water separation. *Adv Mater* 30(9):1704912
43. Li X, Chen Y (2017) Micro-scale feature fabrication using immersed surface accumulation. *J Manuf Process* 28:531–540
44. Li X et al (2018) Mask video projection based stereolithography with continuous resin flow to build digital models in minutes. In: ASME 2018 13th international manufacturing science and engineering conference. American Society of Mechanical Engineers
45. Zhou C, Chen Y, Waltz RA (2009) Optimized mask image projection for solid freeform fabrication. In: ASME 2009 international design engineering technical conferences and computers and information in engineering conference. American Society of Mechanical Engineers
46. Li X et al (2018) 3D printing temporary crown and bridge by temperature controlled mask image projection stereolithography. *Procedia Manuf* 26:1023–1033
47. Zhou C et al (2013) Digital material fabrication using mask-image-projection-based stereolithography. *Rapid Prototyp J* 19(3):153–165
48. Song X et al (2015) Ceramic fabrication using mask-image-projection-based stereolithography integrated with tape-casting. *J Manuf Process* 20:456–464
49. Song X et al (2017) Piezoelectric component fabrication using projection-based stereolithography of barium titanate ceramic suspensions. *Rapid Prototyp J* 23(1):44–53
50. Frisch U, Hasslacher B, Pomeau Y (1986) Lattice-gas automata for the Navier–Stokes equation. *Phys Rev Lett* 56(14):1505
51. Zissi S et al (1996) Stereolithography and microtechniques. *Microsyst Technol* 2(2):97–102
52. Jacobs PF (1992) Rapid prototyping & manufacturing: fundamentals of stereolithography. Society of Manufacturing Engineers, Dearborn
53. Griffith ML, Halloran JW (1993) Freeform fabrication of ceramics via stereolithography. *J Am Ceram Soc* 79(10):2601–2608
54. Song X et al (2017) Porous structure fabrication using a stereolithography-based sugar foaming method. *J Manuf Sci Eng* 139(3):031015
55. Hamad AJ (2017) Size and shape effect of specimen on the compressive strength of HPLWFC reinforced with glass fibres. *J King Saud Univ Eng Sci* 29(4):373–380
56. Miller RG Jr (1997) Beyond ANOVA: basics of applied statistics. Chapman and Hall, Boca Raton
57. Jordan MM et al (2008) Influence of firing temperature and mineralogical composition on bending strength and porosity of ceramic tile bodies. *Appl Clay Sci* 42(1–2):266–271
58. Deng XG et al (2016) Effects of firing temperature on the microstructures and properties of porous mullite ceramics prepared by foam-gelcasting. *Adv Appl Ceram* 115(4):204–209
59. Rice RW (1993) Comparison of stress concentration versus minimum solid area based mechanical property-porosity relations. *J Mater Sci* 28(8):2187–2190
60. Heunisch A, Dellert A, Roosen A (2010) Effect of powder, binder and process parameters on anisotropic shrinkage in tape cast ceramic products. *J Eur Ceram Soc* 30(16):3397–3406
61. Boccaccini AR, Trusty PA (1998) In situ characterization of the shrinkage behavior of ceramic powder compacts during sintering by using heating microscopy. *Mater Charact* 41(4):109–121
62. Hollister SJ (2009) Scaffold design and manufacturing: from concept to clinic. *Adv Mater* 21(32–33):3330–3342
63. Kwok T-H et al (2017) Mass customization: reuse of digital slicing for additive manufacturing. *J Comput Inf Sci Eng* 17(2):021009
64. Xu K, Kwok T-H, Chen Y (2016) A reverse compensation framework for shape deformation in additive manufacturing. In: ASME 2016 11th international manufacturing science and engineering conference. American Society of Mechanical Engineers
65. Leung Y-S et al (2019) Challenges and status on design and computation for emerging additive manufacturing technologies. *J Comput Inf Sci Eng* 19(2):021013
66. Chung I-H et al (2009) Stem cell property of postmigratory cranial neural crest cells and their utility in alveolar bone regeneration and tooth development. *Stem Cells* 27(4):866–877
67. Leucht P et al (2008) Embryonic origin and Hox status determine progenitor cell fate during adult bone regeneration. *Development* 135(17):2845–2854